Supplementary Information (SI) for Nanoscale.
This journal is © The Royal Society of Chemistry 2026

Supporting Information

Enhanced stability and ultraviolet photodetection performance in $CsPbBr_3$ nanoplatelets via FA doping

Le Luo[a], *Xiaoming Mo*[a]*, *Yusheng Song*[a], *Zhentao Du*[b], *Sheng Cao*[a], *Jinju Zheng*[c]*, *Bingsuo Zou*[a,b], *and Jialong Zhao*[a]*

[a] School of Physical Science and Technology, State Key Laboratory of Featured Metal Materials and Life-cycle Safety for Composite Structures, Guangxi Key Laboratory of Processing for Non-ferrous Metals and Featured Materials, Guangxi University, Nanning 530004, China;

[b] School of Resources, Environment and Materials, Guangxi University, Nanning 530004, China;

[c] College of Information Technology, Jilin Engineering Research Center of Optoelectronic Materials and Devices, Jilin Normal University, Siping 136000, China.

Corresponding Authors
*E-mail: xmmo@gxu.edu.cn (X. M. M.)
*E-mail: zhengzhao2007@163.com (J. J. Z.)
*E-mail: zhaojl@ciomp.ac.cn (J. L. Z.)

Characterizations

Steady-state photoluminescence (PL) spectra of the colloidal solutions and temperature-dependent PL spectra of the films were acquired on a Horiba Jobin Yvon Fluorolog-3 spectrofluorometer with 365 nm excitation. Time-resolved PL (TRPL) decay curves were measured using a 368 nm pulsed laser. UV-visible absorption spectra of the colloidal solutions were recorded using a Shimadzu UV-2700 spectrophotometer. PL quantum yields (PLQYs) of the samples were determined using a Hamamatsu Photonics Quantaurus-QY (C11347) system under 365 nm excitation. In-situ PL spectra were collected by an Ocean Optics HL-3 plus fiber optic spectrometer. Transmission electron microscope (TEM) images were obtained on an FEI Tecnai G2 F30 microscope operating at 300 kV. X-ray photoelectron spectroscopy (XPS) and ultraviolet photoelectron spectroscopy (UPS) analysis were performed using an ESCALAB 250Xi system with monochromatic Al Kα radiation. The valence band maximum (VBM) levels of NPLs were assessed by the UPS measurement using a He I photon source (21.22 eV). X-ray diffraction (XRD) patterns were collected on a Rigaku D/MAX 2500V diffractometer with Cu Kα radiation (λ = 1.540 Å). Fourier-transform infrared (FTIR) spectra were measured using a Shimadzu IRTracer-100 spectrometer. Hitachi SU8000 acquired cross-sectional scanning electron microscope (SEM) images.

Device Measurements

Electrical measurements of the devices were performed using a Keithley 4200 semiconductor characterization system, with a purpose-designed sample stage. A laser diode (wavelength 365 nm, tunable light intensity) was used as the illumination source and was directed from the back of the devices. Typical I-V curves were measured with voltage-sweeping mode from -0.5 V to 0.5 V. The I-T response curves under different light intensities were measured at a 0 V bias voltage. The response time of the device was measured using a Keithley 6517B. All devices were stored in ambient conditions without encapsulation during measurement.

DFT calculations

Density Functional Theory (DFT) Calculation. The Gaussian 16 program package was used to calculate the geometric and electronic properties of the additives using the B3LYP functional and the 6-31G(d) basis set. GaussView 6.0 was used to visualize and plot the electrostatic potential surfaces (ESPs). DFT calculations for perovskite were performed using the Vienna ab initio simulation package (VASP). The electron-ion interactions are described using the projector augmented wave (PAW)method, and the exchange-correlation potential is approximated by the Perdew-Burke-Ernzerhof (PBE) flooding approximation of the generalised gradient approximation (GGA). Both geometry optimization and electronic structure calculations are performed based on a 2×2×2 supercell of $CsPbBr_3$. The convergence thresholds for energy and force are 1.0×10^{-5} eV and 0.02 eV/Å, respectively, and the plane wave has a cut-off energy of 500 eV. The adsorption energy (E_{ads}) can be calculated using the following formula:

$$E_{ads} = E_{total} - E_{perovskite} + E_{ligand}\#(3)$$

where E_{total} is the total energy of the adsorption system, $E_{perovskite}$ is the energy of the $CsPbBr_3$ surface, and E_{ligand} is the energy of the organic ligand in an isolated state. Furthermore, the calculated formation energy (E_f) for the bromine vacancies is:

$$E_f = E_{vacancy} - E_{initial} + E_{Br} \# (4)$$

where $E_{vacancy}$, $E_{initial}$, and E_{Br} are the total energy of the perovskite molecular system with defects, the perovskite molecular system (initial structure calculated by defects), and bromine (per atom), respectively.

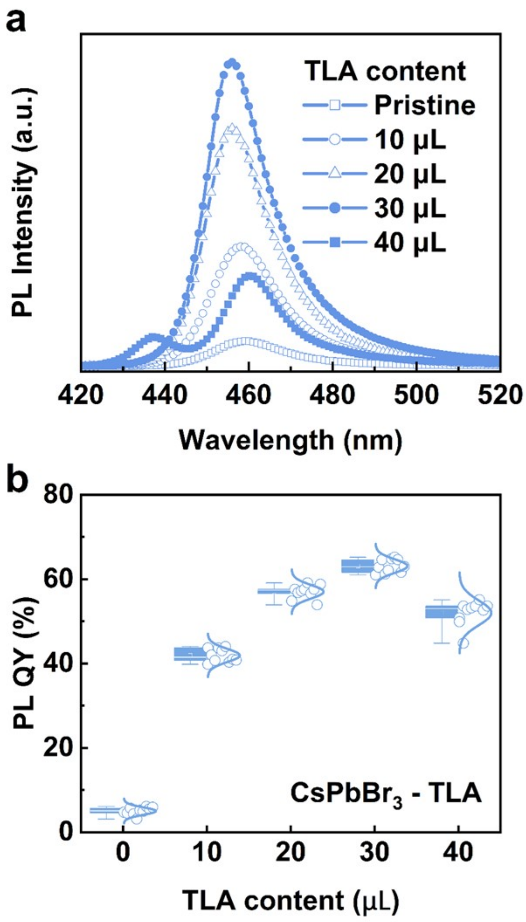

Figure S1. (a) PL spectra and **(b)** statistical PLQY distribution for ten synthetic batches of $CsPbBr_3$ NPLs treated with different amounts of TLA ligands.

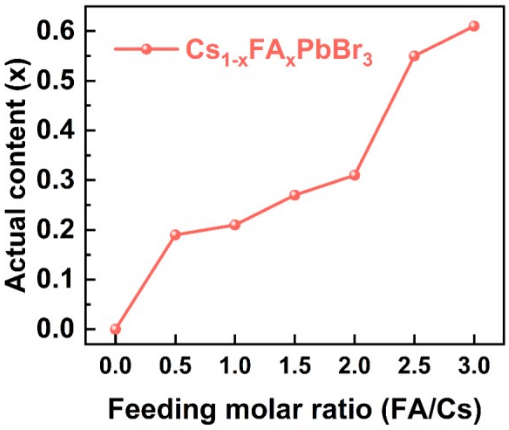

Figure S2. The actual content of FA^+ cations in $Cs_{1-x}FA_xPbBr_3$-TLA NPLs at different feeding molar ratios of FA^+/Cs^+, using EDS measurement.

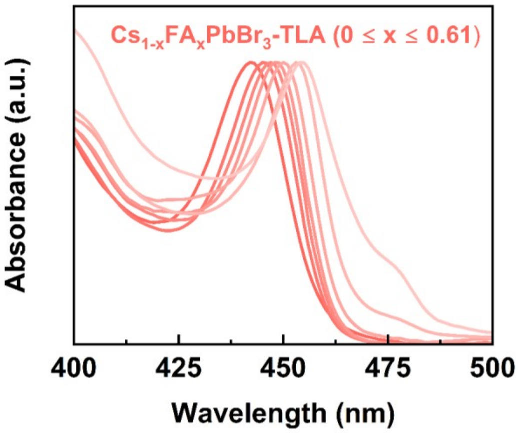

Figure S3. UV-vis absorption spectra of the $Cs_{1-x}FA_xPbBr_3$-TLA NPLs ($0 \leq x \leq 0.61$).

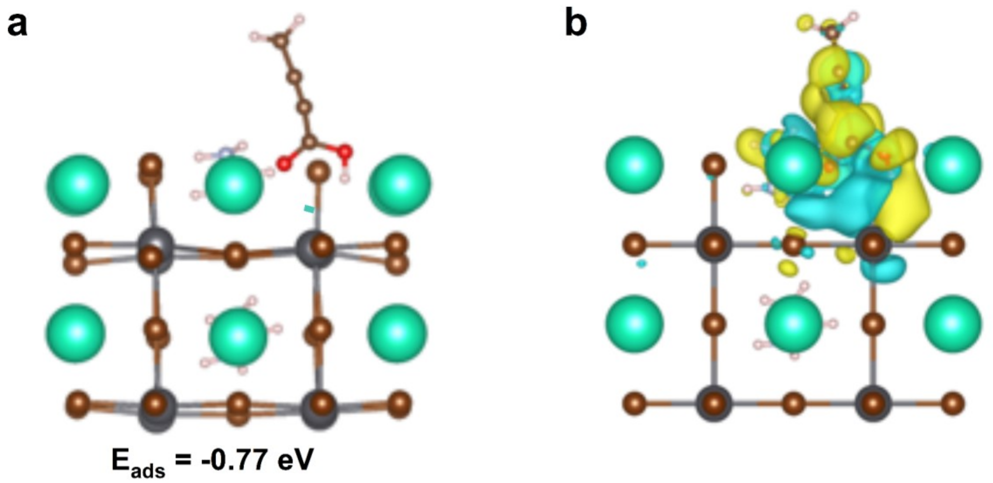

Figure S4. (a) DFT models of the adsorption between the TLA ligand and $Cs_{0.73}FA_{0.27}PbBr_3$ NPLs. **(b)** Charge density difference contour of the TLA ligands on the $Cs_{0.73}FA_{0.27}PbBr_3$ NPLs surface.

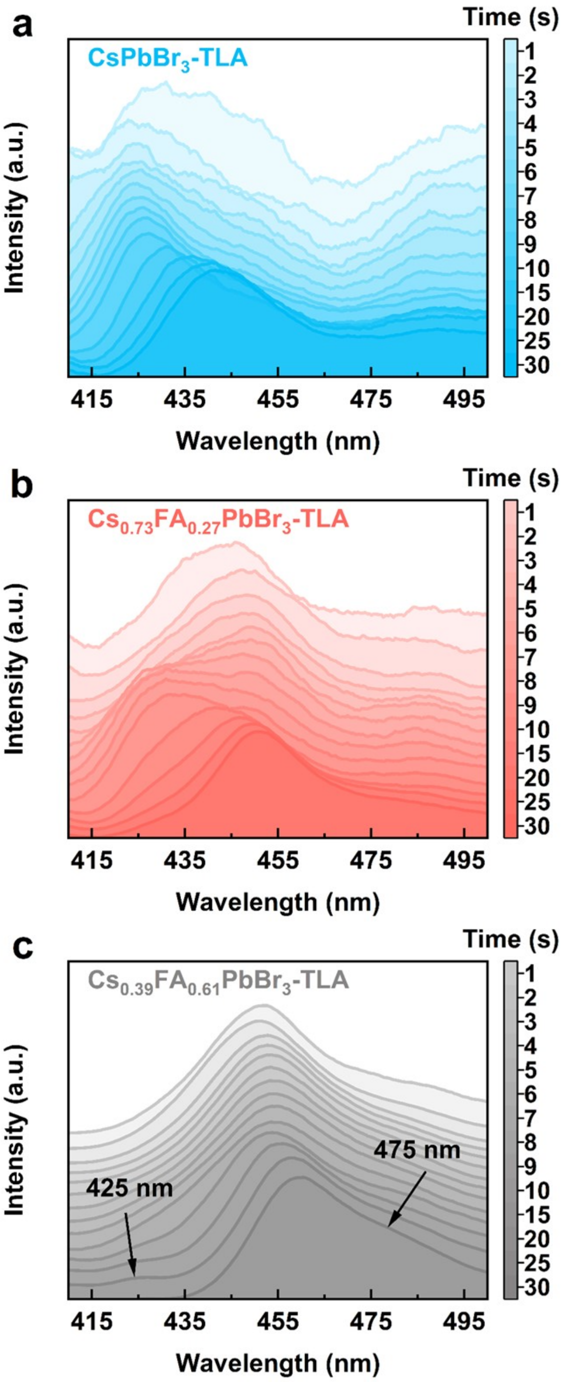

Figure S5. In-situ spectroscopic monitoring during the synthesis of the (a) $CsPbBr_3$-TLA, (b) $Cs_{0.73}FA_{0.27}PbBr_3$-TLA, and (c) $Cs_{0.39}FA_{0.61}PbBr_3$-TLA NPLs for the first 30 seconds.

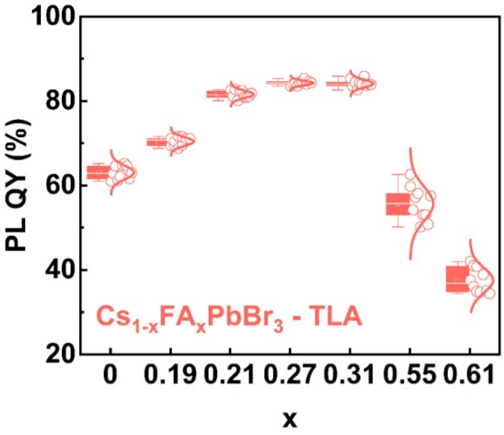

Figure S6. Statistical distribution of PLQYs across ten batches for the $Cs_{1-x}FA_xPbBr_3$-TLA NPLs with different FA^+ content.

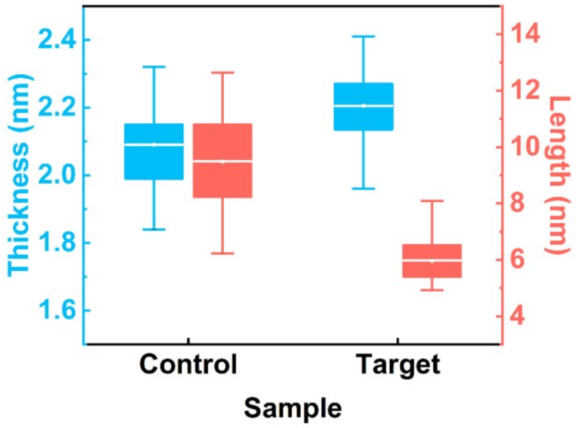

Figure S7. The statistical size chart of the lateral (thickness) and longitudinal (length) dimensions of the Control and Target NPLs.

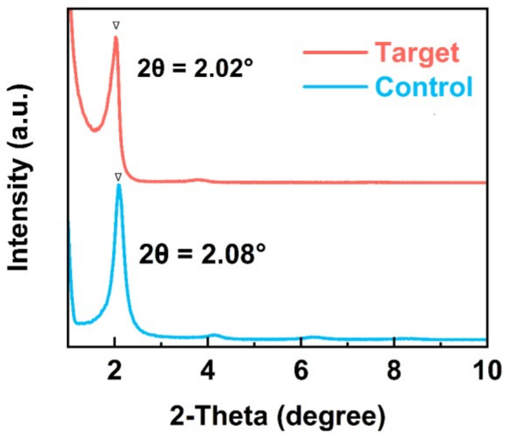

Figure S8. Small-angle XRD patterns of the Control and Target NPLs.

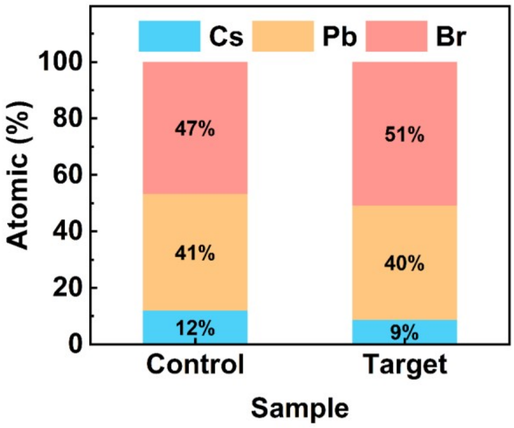

Figure S9. The statistical chart of the contents of Cs, Pb, and Br elements in Control and Target NPLs as tested by XPS measurements.

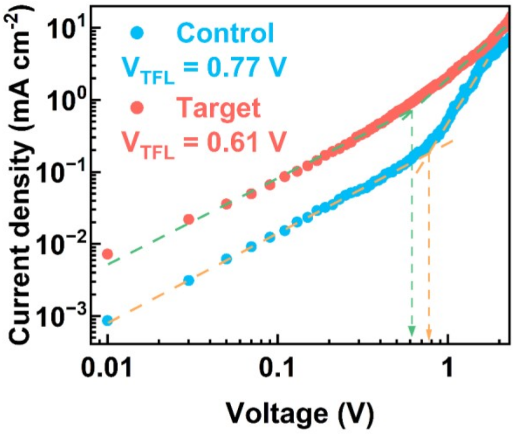

Figure S10. The SCLC plot of an electron-only device (EOD) with the structure ITO/SnO_2/perovskite NPLs/TPBi/Ag.

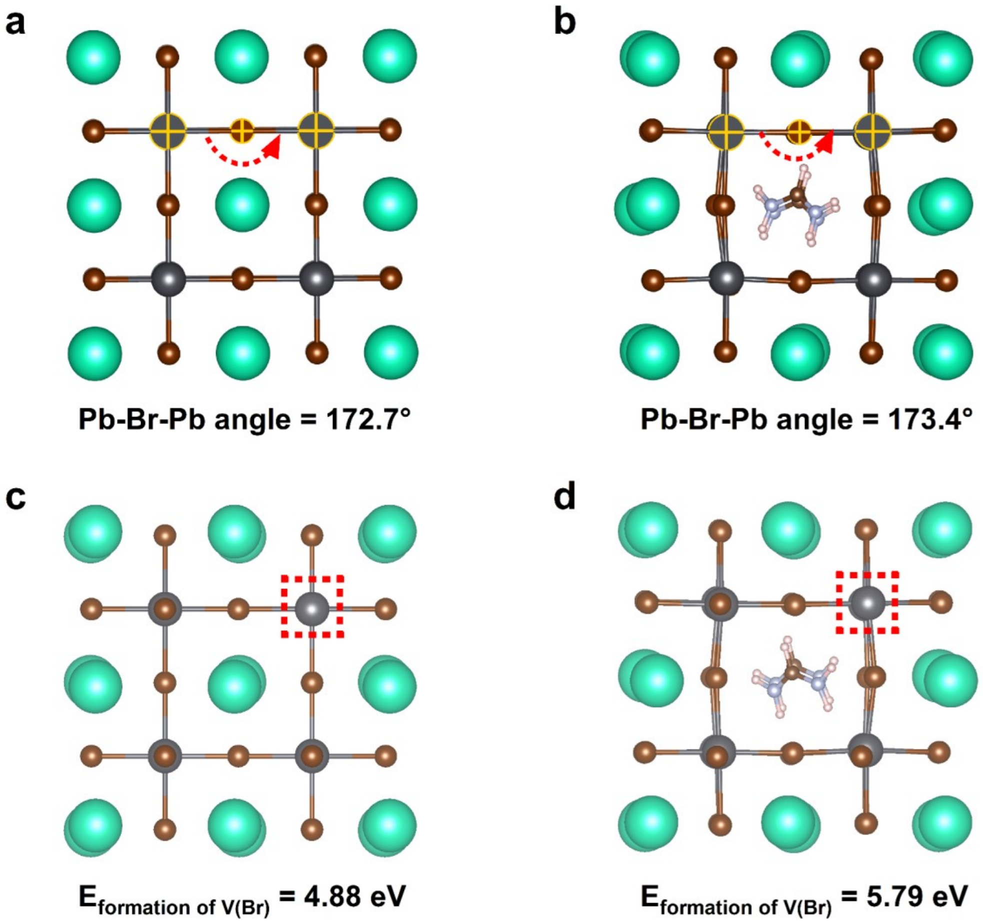

Figure S11. The calculated Br-Pb-Br bond angle and Br-Pb bond lengths of the **(a)** $CsPbBr_3$ and **(b)** $Cs_{0.73}FA_{0.27}PbBr_3$ NPLs. Calculated formation energy of Br vacancies on the surface of **(c)** $CsPbBr_3$, and **(d)** $Cs_{0.73}FA_{0.27}PbBr_3$ NPLs.

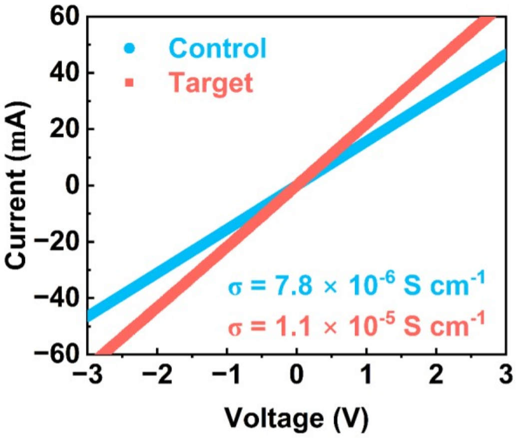

Figure S12. Electrical conductivity tests of the Control and Target NPL films.

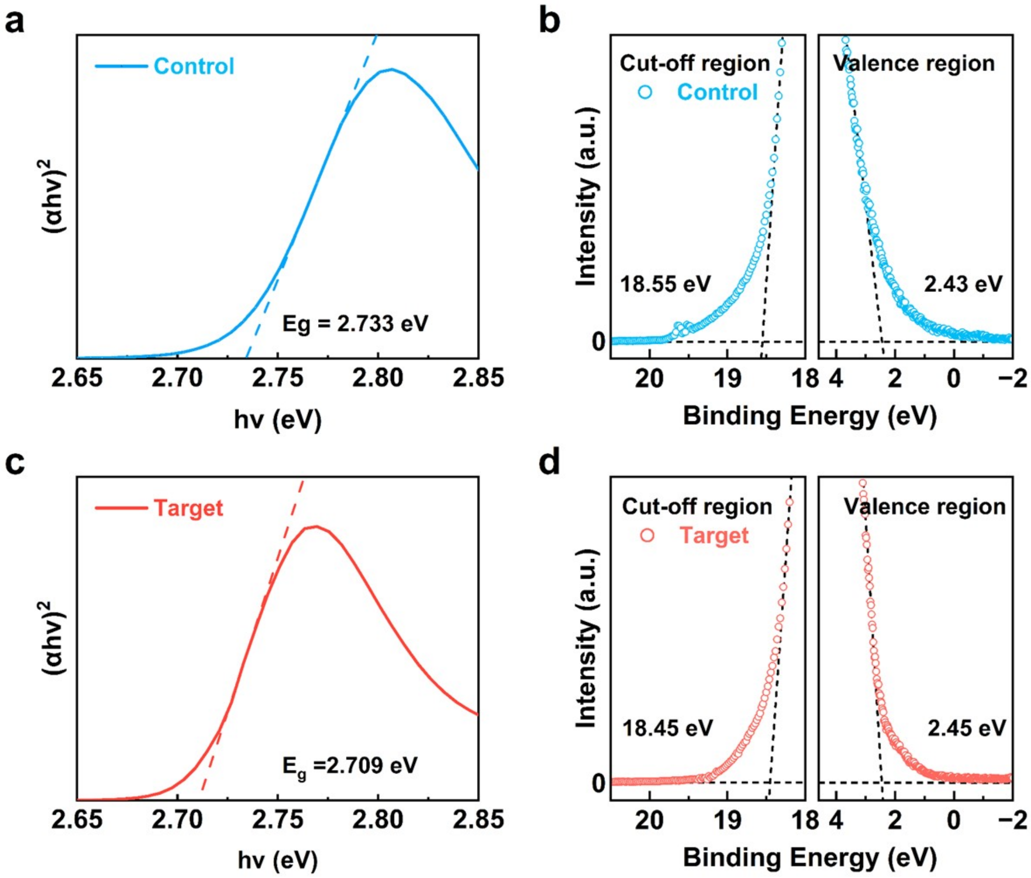

Figure S13. The Tacu-plot curve of the (a) Control and (c) Target NPLs. The UPS energy spectrum of the (b) Control and (d) Target NPLs.

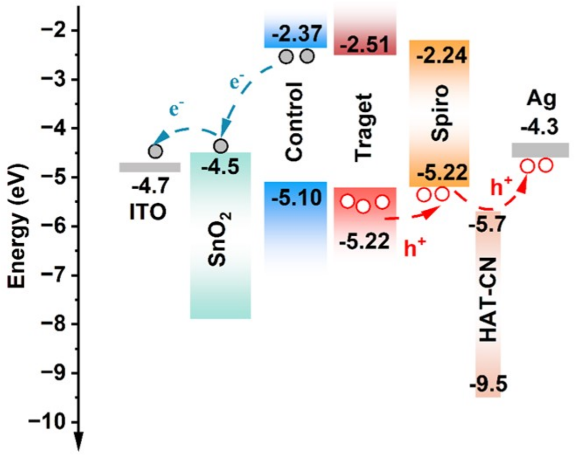

Figure. S14. Schematic energy band structure of the PDs.

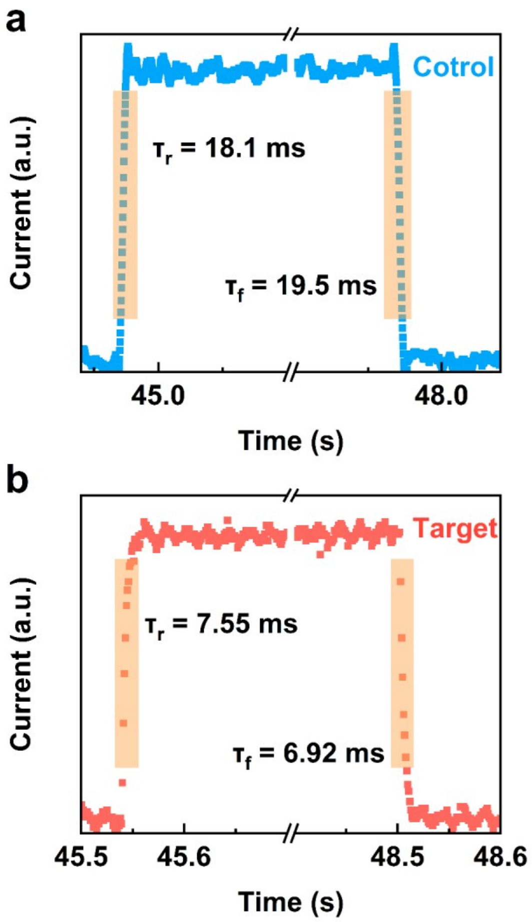

Figure S15. The response time of the PDs based on (a) Control and (b) Target NPLs under a 0 V bias voltage and a 0.58 mW cm^{-2} UV irradiation (365 nm).

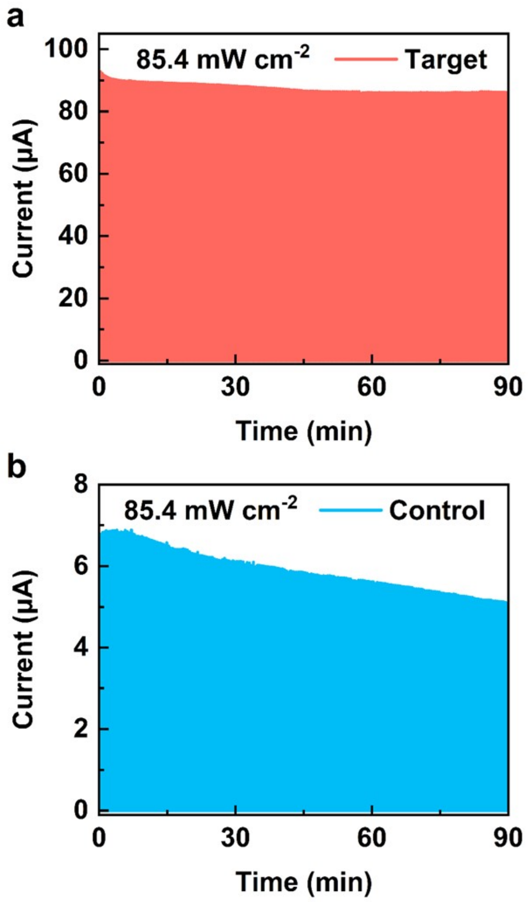

Figure S16. Time-dependent current (I-T) curve of the PDs with (a) the Control and (b) the Target NPLs after approximately 200 switching cycles under 365 nm UV light intensity of 85.4 mW cm^{-2}.

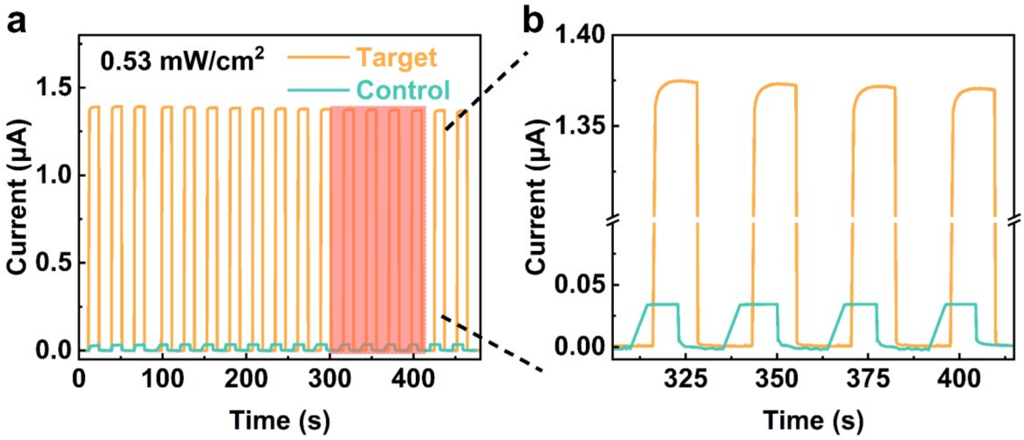

Figure S17. After being placed in the air environment for 30 days, **(a)** the photocurrent response curves and **(b)** their local magnified images of the PDs with the Control and Target NPLs under 365 nm UV light intensity of 0.53 mW cm^{-2}.

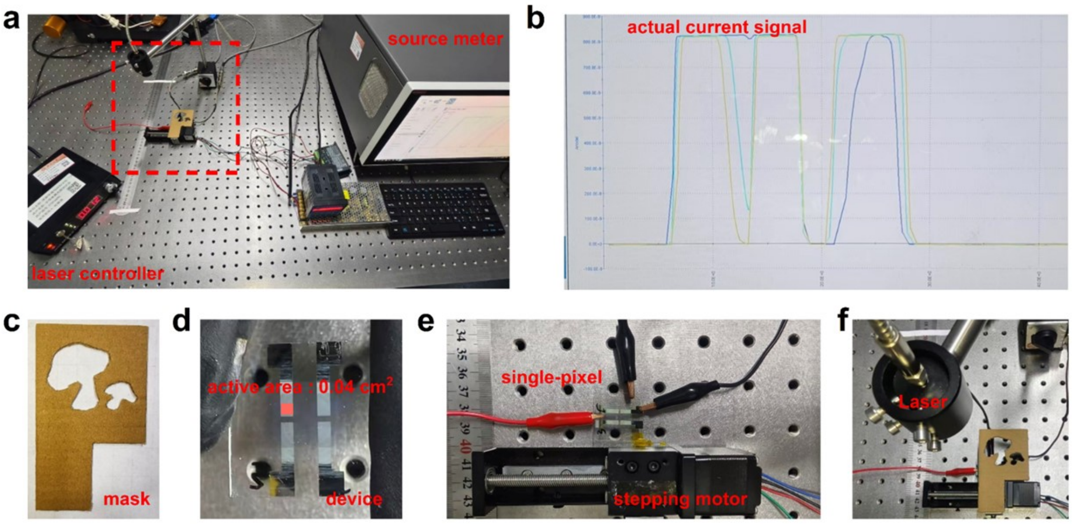

Figure S18. Single-pixel UV imaging system and performance verification based on modified CsPbBr3 nanoplatelets. (a) Optical photo of the single-pixel imaging system, including semiconductor analyzer, laser controller, stepper motor, mask plate and single-pixel detector module. (b) Representative photocurrent response curve collected during imaging. (c) Optical photo of the target mask plate (with "mushroom" pattern) used for imaging. (d) Optical photo of the fabricated single-pixel detector, with the effective detection area indicated by the red frame. (e) Single-pixel detector module connected to the semiconductor analyzer. (f) Partial magnified photo of the single-pixel module corresponding to the red dashed box area in (a).

Ultraviolet detection imaging demonstration:

Stage 1: Connect the as-prepared detector to the semiconductor parameter analyzer, and mount it parallel to the experimental platform with the glass surface facing upward to receive optical signals.

Stage 2: Adjust the positions of the laser source and the device to ensure the laser beam fully illuminates the effective active area during operation. Secure the prefabricated mask to the designated position of the stepper motor. Place the stepper motor between the laser source and the device, and record its initial position (the effective stroke of the stepper motor is approximately 55 mm, with a single stroke taking around 40 s).

Stage 3: Launch the testing program. Activate the stepper motor to drive the mask to horizontal motion under continuous laser irradiation. One complete movement yields a set of time-dependent current (I-T) curves. Translate the mask by 1 mm along the direction perpendicular to its moving direction after each scan; ultimately, 50 sets of scanning data are acquired.

Stage 4: Data processing: Extract test time points at equal intervals, compute the average current magnitude for each dataset at the corresponding time, and plot a 50 × 55 pixels matrix correlated with time and current intensity. The matrix is visualized as a heat map to generate the final reconstructed image.

Table S1. Optical properties of $CsPbBr_3$ NPLs that were synthesized with different TLA ligand content.

Ligand content (µL)	**Peak (nm)**	**FWHM (nm)**	**PL QY (%)**
0 (Pristine NPLs)	**459**	**19.5**	**5.0**
10	458	19.2	41.9
20	456	18.5	57.0
30 (Control NPLs)	**456**	**18.0**	**63.1**
40	438/460	12.0/16.4	52.0

Table S2. Optical properties of $Cs_{1-x}FA_xPbBr_3$-TLA NPLs that were synthesized with different FA^+/Cs^+ ratios.

Sample	Peak (nm)	FWHM (nm)	PL QY (%)	Band gap (eV)
0.0 (Control NPLs)	**456**	**18.0**	**63.1**	**2.733**
0.5	458	16.5	70.4	2.721
1.0	459	15.9	81.6	2.714
1.5 (Target NPLs)	**460**	**15.6**	**84.3**	**2.709**
2.0	463	15.7	84.1	2.695
2.5	467	19.5	55.7	2.655
3.0	473	18.9	37.6	2.588

Table S3. The calculated trap density (n_{trap}) and charge mobility (μ) of Control and Target NPL films.

Sample	**V_{TFL} (V)**		**n_{trap} ($\times 10^{16}$ cm^3)**		**μ ($\times 10^{-4}$ cm^2 V^{-1} s^{-1})**	
	EOD	**HOD**	**EOD**	**HOD**	**EOD**	**HOD**
Control	0.77	2.08	3.14	8.47	0.23	3.62
Target	0.61	1.75	2.48	7.13	1.34	8.53

Table S4. The TRPL decay fitting results of the Control and Target NPLs colloidal solutions.

Sample	**A_1**	**τ_1**	**A_2**	**τ_2**	**τ_{ave} (ns)**
Control	66.2%	3.86	33.8%	7.98	5.25
Target	79.0%	5.95	21.0%	13.19	7.47

Table S5. The detection performance of PDs based on the Control and Target NPLs under 365 nm UV light at different light powers.

Device	Light intensity (mW cm^{-2})	I_{photo} (μA)	LDR (dB)	K ($\times10^3$)	R_λ (A W^{-1})	D^* (Jones)	τ_{rise}/τ_{fall} (ms)
Control	0.53	0.095	55	0.57	0.0045	1.23×10^{11}	18.1/19.5
	3.13	0.42	68	2485	0.0033	9.10×10^{10}	-
	7.73	0.89	74	5273	0.0029	7.82×10^{10}	-
	11.0	1.17	76	6941	0.0027	7.24×10^{10}	-
	17.3	1.78	80	10584	0.0026	7.01×10^{10}	-
	36.0	3.67	86	21882	0.0025	6.98×10^{10}	-
Target	0.53	1.88	90	30.2	0.0891	3.99×10^{12}	7.55/6.92
	3.13	6.54	100	105	0.0523	2.34×10^{12}	-
	7.73	14.2	107	229	0.0461	2.07×10^{12}	-
	11.0	19.9	110	320	0.0453	2.03×10^{12}	-
	17.3	30.5	113	490	0.0441	1.98×10^{12}	-
	36.0	63.2	120	1015	0.0440	1.97×10^{12}	-

Table S6. The changes in the detection performance of the PDs, based on the Control and Target NPLs, after 30 days of exposure to 365 nm UV light at an intensity of 0.53 mW cm^{-2}.

Device	**I_{photo} (×10^{6}A)**	**I_{dark} (×10^{-11} A)**	**LDR (dB)**	**K (×10^3)**	**R_λ (A W^{-1})**	**D^* (Jones)**
Control	0.034	259.9	22	0.013	0.0015	1.03×10^{10}
Target	1.37	17.7	78	7.7	0.0649	1.73×10^{12}

Note S1.

The Urbach energies (E_U) of the samples were extracted by fitting the exponential part of the Urbach tail according to the following equation:

$$\alpha(E) = \alpha_0 \exp\left[\sigma(T)\frac{E - E_0}{k_B T}\right]\#(1)$$

where $\alpha(E)$ is the absorption coefficient as a function of photon energy E, E_0, and α_0 are the characteristic parameters of the material, $\sigma(T)$ is the steepness parameter, k_B is the Boltzmann constant, and T is the thermodynamic temperature.

Note S2.

The trap densities were calculated using the equation:

$$N_t = \frac{2\varepsilon\varepsilon_0 V_{TFL}}{eL^2} \#(2)$$

where ε and ε_0 represent the dielectric constant and vacuum dielectric constant, V_{TFL} is the trap-filling limit voltage in the single-carrier device, *e* is the elementary charge, and *L* is the thickness of the film, 50 nm for the perovskite film.

Note S3.

The exciton binding energy of the Control and Target NPLs can be calculated by fitting the following Arrhenius formula:

$$I(t) = \frac{I_0}{1 + Aexp(-\frac{E_b}{K_B T})} \#(3)$$

where *I(t)* is the PL intensity at different temperatures, I_0 is the intensity at 0 K, *A* is a constant, E_b is the exciton binding energy, and K_B is the Boltzmann constant.

Note S4.

The switch ratio (*K*) of the photodetectors was calculated as:

$$K = \frac{I_{on} - I_{off}}{I_{off}} \#(4)$$

where I_{on} is photocurrent and I_{off} is dark current.

Note S5.

The linear dynamic range (*LDR*) of the photodetectors was calculated as:

$$LDR = 20\log\frac{J_{max}}{J_{min}} \#(5)$$

where J_{on} and J_{on} are the maximum and the minimum detectable current densities, respectively.

Note S6.

The responsivity (R_{λ}) of the photodetectors was calculated as:

$$R_{\lambda} = \frac{I_{on} - I_{off}}{PA} \#(6)$$

where I_{on} is the photocurrent, I_{off} is the dark current, *P* is the optical power of the laser, and $A = 0.04\ cm^2$ is the active area of the device.

Note S7.

The specific detectivity (D^*) of the photodetectors was calculated as:

$$D^* = \frac{R_{\lambda}}{\sqrt{2e\frac{I_{off}}{A}}} \#(7)$$

where *e* is the electron charge, and I_{off} is the dark current, which is considered to be the major noise in the photovoltaic detector. *A* is the effective area of the detector, and R_{λ} is the photoresponsivity at the corresponding wavelength.